

Controllable *in-situ*-oxidization of 3D-networked $\text{Ti}_3\text{C}_2\text{T}_x\text{-TiO}_2$ photodetectors for large-area flexible optical imaging

Da Xiong, Weili Deng^{*}, Guo Tian, Binbin Zhang, Shen Zhong, Yanting Xie, Tao Yang, Haibo Zhao, Weiqing Yang^{*}

Key Laboratory of Advanced Technologies of Materials (Ministry of Education), School of Materials Science and Engineering, Southwest Jiaotong University, Chengdu 610031, PR China

ARTICLE INFO

Keywords:

MXenes
Controllable *in-situ*-oxidization
3D-networked $\text{Ti}_3\text{C}_2\text{T}_x\text{-TiO}_2$
Optical imaging

ABSTRACT

The intrinsic hydrophilicity of MXenes makes a promise for the large-area fabrication of flexible optoelectronic devices. However, the inferior optical absorption and high scattering rate of pure MXenes severely limit its practical application in photodetectors. Here, we demonstrate a controllable *in-situ*-oxidization strategy for the large-scale fabrication of 3D-networked $\text{Ti}_3\text{C}_2\text{T}_x\text{-TiO}_2$ heterostructure for photodetectors. Benefiting from the enhanced optical absorption and the enlarged carrier transport efficiency, this photodetector can achieve 13.3 times performance improvement than that of the pristine $\text{Ti}_3\text{C}_2\text{T}_x$ under 405 nm (8.58 mW) light illumination at 5 V bias. Furthermore, the as-developed 3D-networked $\text{Ti}_3\text{C}_2\text{T}_x\text{-TiO}_2$ photodetectors can be conveniently fabricated into a large-area array ($10 \times 10 \text{ cm}^2$), which can effectively image the shape of “p” letter as well as more complex circular patterns, indicating the huge potential of large-area flexible optical imaging. Evidently, this controllable *in-situ*-oxidization strategy paves a way for the construction of versatile 3D-networked functional materials for electronic devices.

1. Introduction

As an important component of optoelectronic devices, photodetectors possess the ability to convert the optical signal into electrical output via the photoelectric effect, which have widespread applications in our daily life, such as optical communication [1,2], optical imaging [3,4], biomedical imaging [5,6], health and atmospheric monitoring [7,8], and so on. Recently, the booming development of flexible two-dimensional (2D) material-based photodetectors has been achieved due to their extraordinary properties such as high carrier mobility and broadband responsivity [9,10].

MXenes, as an emerging family of 2D transition metal carbides, nitrides, and carbonitrides, are attracting great attention since their discovery in 2011 [11]. Benefiting from the tunable electronic structures induced by their intrinsically abundant terminal groups, MXenes are rich in tunable optical and electrical properties that promote the prosperous development of electronic devices [12–16]. Especially, the intrinsic hydrophilicity of MXenes facilitates the fabrication of large-area devices, overcoming the bottleneck of large-scale fabrication in practical application [17–19]. So far, most of the reported

MXenes-related photodetectors are focused on the metallic $\text{Ti}_3\text{C}_2\text{T}_x$, whose good metallic conductivity and high transparency facilitate its use as a transparent electrode and the formation of Schottky junction when in contact with other semiconductors [20–25]. However, $\text{Ti}_3\text{C}_2\text{T}_x$ shows almost no photoresponse to the optical signal due to its limited absorbance and high scattering rate [26–28], which greatly hinders its application in photodetectors. In this regard, oxidized MXenes and MXenes/perovskite nanocomposites have been proved to be the representative strategy for enhancing device performance, ascribing to the synergistic effect of high absorbance of derivative TiO_2 /perovskite and high carrier mobility of MXenes [29–31]. In contrast, the air-oxidized MXenes provide a convenient strategy to enhance the optical absorption and overturn the disadvantage of air-induced oxidation of MXenes. However, the reported partially oxidized MXenes- TiO_2 nanocrystal composite still shows a slow response speed and limited responsivity [30].

In view of these problems, a three-dimensional (3D)-networked $\text{Ti}_3\text{C}_2\text{T}_x\text{-TiO}_2$ heterostructure was constructed to form the high-performance photodetectors by a controllable *in-situ*-oxidization strategy. In contrast with the previous oxidization strategy, the controllable

^{*} Corresponding authors.

E-mail addresses: weili1812@swjtu.edu.cn (W. Deng), wqyang@swjtu.edu.cn (W. Yang).

in-situ-oxidation derivative 2D TiO₂ nanosheets connected with the separated Ti₃C₂T_x nanosheets, which constitutes a 3D-networked structure. The results show this 3D-networked structure can achieve a 13.3 times promotion of photoresponsivity than that of pristine Ti₃C₂T_x photodetectors due to the improvement of optical absorption for the existence of TiO₂ and the enhanced separation of generated excitons for the excellent electrical conductivity of Ti₃C₂T_x nanosheets. In addition, the tight connection between Ti₃C₂T_x and TiO₂ can further enhance the carrier transport efficiency for the efficient conductive pathway. Combined with the hydrophilicity of MXenes, a large-area 3D-networked Ti₃C₂T_x-TiO₂ photodetectors array can be conveniently prepared to clearly restore the shaped light and realize optical imaging. Thus, this controllable *in-situ*-oxidation strategy provides a feasible way to construct 3D-networked MXenes-derivative heterostructure for electronic devices.

2. Results and discussions

Fig. 1 schematically illustrated the structure design of functional materials and its large area fabrication process. Due to the hydrophilicity of MXenes, the functional materials can be uniformly dispersed in the aqueous solution (Fig. S1), and thus the functional layer can be easily drop-casted onto the flexible substrate with a patterned back electrode to fabricate scalable photodetectors array as depicted in Fig. 1a. Compared with other substrate, paper substrate shows good hydrophilicity (Fig. S2) and excellent flexibility with lower cost [32–34]. As a result, the large area of high-quality functional material film can be successfully fabricated on the paper substrate to form the flexible photodetectors array. In detail, the MXenes-based

photodetectors were formed by the functional layers of 3D-networked Ti₃C₂T_x-TiO₂ heterostructure, sputtered Ag electrodes, and the flexible paper substrate (Fig. 1b). The detailed fabrication process and schematic diagram can be seen in the experimental section and Fig. S3. As shown in Fig. 1c, the controllable oxidation derivative TiO₂ nanosheets were inserted vertically across the layered Ti₃C₂T_x nanosheets to form the 3D-networked Ti₃C₂T_x-TiO₂ heterostructure. And such heterostructure can be rapidly and efficiently prepared by the controllable *in-situ*-oxidation of Ti₃C₂T_x with morphology directing reagent NaBF₄. The results of scanning electron microscopy (SEM) and transmission electron microscopy (TEM) were further verified the successful fabrication of 3D-networked Ti₃C₂T_x-TiO₂ heterostructure (Fig. 1d–e). The Ti source of 2D TiO₂ can be easily obtained from the Ti₃C₂T_x nanosheets without any additive during the process of controllable *in-situ*-oxidation (Fig. S4), which enhances the interfacial affinity and reduces the defects [35]. Due to the derivative TiO₂, the photoinduced carriers can be collected more efficiently through Ti₃C₂T_x nanosheets for their excellent electrical properties (Fig. 1f) and its work function was lower than that of TiO₂ (Fig. S5), and the photocurrent can be tuned by different oxidation times (Fig. 1g). Most importantly, the derivative TiO₂ nanosheets can bridge the separated Ti₃C₂T_x nanosheets, providing more electron conduction pathways and decreasing the electron scattering in Ti₃C₂T_x nanosheets [36], and thus improving the electron collection efficiency, as illustrated in Fig. 1h–i and Fig. S6. On this basis, compared with pristine Ti₃C₂T_x, the 3D-networked Ti₃C₂T_x-TiO₂ heterostructure can greatly improve the performance on account of the enhanced optical absorption and carrier collect efficiency, which lays the foundation for the development of high-performance MXene-based photodetectors.

For deep insight into the functionality of the as-prepared 3D-

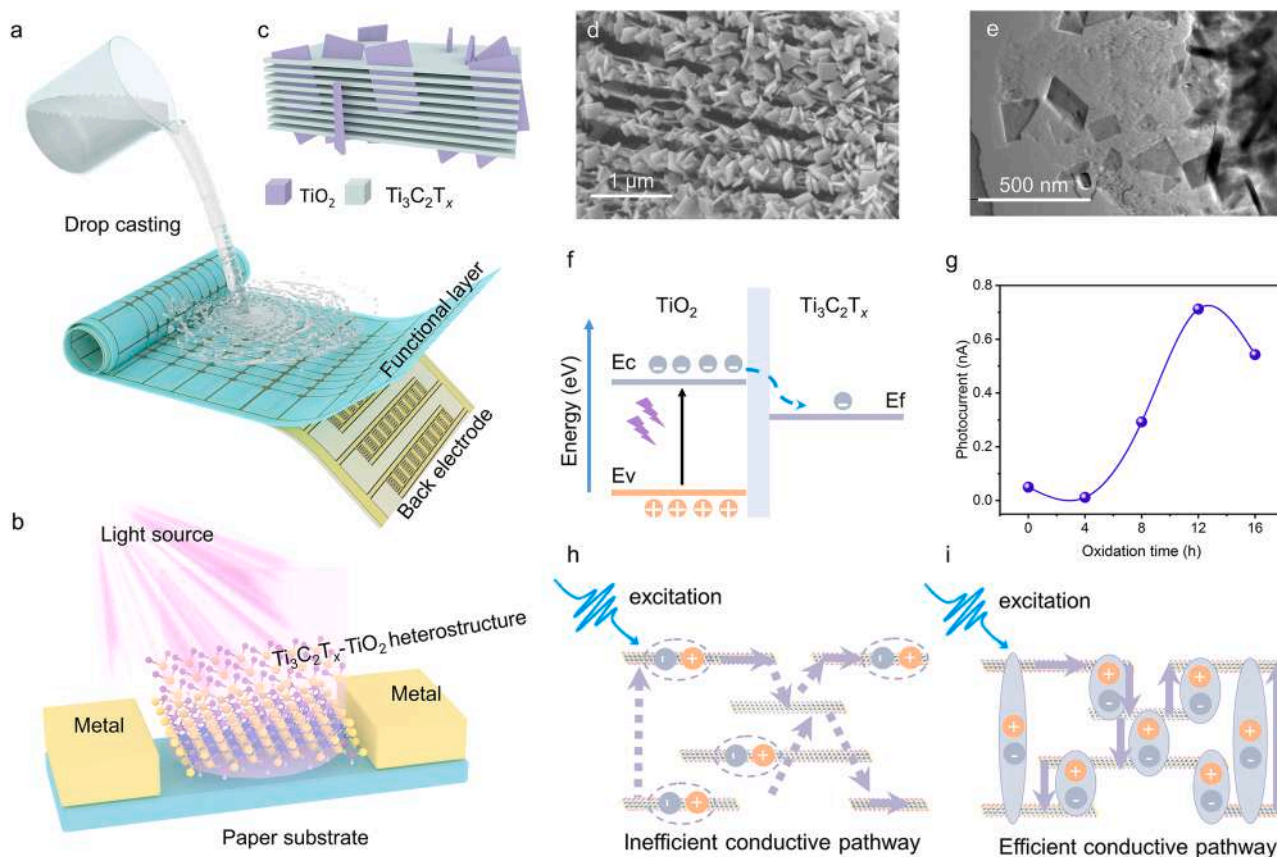


Fig. 1. Schematic illustration of functional materials and mechanism of photoelectric performance improvement. a, Large-area fabrication process of scalable devices. b, Enlarged device schematic diagram. c, Schematic diagram of 3D-networked Ti₃C₂T_x-TiO₂. d, SEM image of 3D-networked Ti₃C₂T_x-TiO₂ (magnification in 30,000 times). e, TEM image of 3D-networked Ti₃C₂T_x-TiO₂. f, Schematic band alignments, and carrier flow at Ti₃C₂T_x-TiO₂ interfaces. g, Photoelectric output comparison of different oxidation times. h–i, Different carrier transport processes over Ti₃C₂T_x (h) and 3D-networked Ti₃C₂T_x-TiO₂ heterostructure (i).

networked $\text{Ti}_3\text{C}_2\text{T}_x\text{-TiO}_2$ heterostructure, the relative confirmatory materials were exploited and characterized. After the etching of Ti_3AlC_2 , the production was further treated by the hydrothermal oxidation with different processes, and the 3D-networked $\text{Ti}_3\text{C}_2\text{T}_x\text{-TiO}_2$ heterostructure could be obtained due to the presence of morphology directing reagent. Obviously, the successful etching of Ti_3AlC_2 and the fabrication of 3D-networked $\text{Ti}_3\text{C}_2\text{T}_x\text{-TiO}_2$ have been confirmed by the SEM images in Figs. S7 and 2a–b. As a result, the controllable oxidation derivative TiO_2 nanosheets bridged the separated $\text{Ti}_3\text{C}_2\text{T}_x$ nanosheets to construct the anticipant 3D network, which was further verified by the TEM result depicted in Fig. 2c. The FFT pattern of the TEM confirms that the interplanar crystal spacing of 0.26 nm ($\text{Ti}_3\text{C}_2\text{T}_x$) and 0.37 nm (TiO_2). For the hydrothermal method, temperature is an important parameter to modulate the microstructure of the materials. Thus, we performed the hydrothermal process under different temperatures of 120 °C, 160 °C, and 200 °C, respectively. The results show that the product can keep at a good shape of 3D-networked structure at 160 °C (Fig. S8), similar results can also be confirmed by the XRD pattern of hydrothermal products under different temperatures (Fig. S9). Meanwhile, the content of TiO_2 increased with the prolonging of reaction time as shown in Fig. S10, thus the 3D network can be controllably regulated by the reaction time. The

elemental mapping imaging of production further proved the successful etching of Ti_3AlC_2 and the formation of $\text{Ti}_3\text{C}_2\text{T}_x\text{-TiO}_2$ heterostructure, corresponding to a small amount of Al and the distribution of O in Figs. S11–S12.

In addition, the various chemical terminal species of $\text{Ti}_3\text{C}_2\text{T}_x$ were further characterized via Raman spectroscopy to verify the formation of $\text{Ti}_3\text{C}_2\text{T}_x\text{-TiO}_2$ heterostructure. In the range of Raman shift from 100 to 800 cm^{-1} , the additional peaks can be assigned to the vibrational mode of Eg of $\text{Ti}_3\text{C}_2\text{F}_2$, $\text{Ti}_3\text{C}_2(\text{OH})_2$, and A1g of $\text{Ti}_3\text{C}_2\text{O}_2$, indicating the existence of terminal groups and the successful etching of Ti_3AlC_2 [37]. Besides, the oxidation derivative TiO_2 was confirmed by the extra Raman shift of $\sim 150\text{ cm}^{-1}$ as shown in Fig. 2d [38]. Meanwhile, two favorable characterizations of X-ray diffraction (XRD) and X-ray photoelectron spectroscopy (XPS) were employed to investigate the crystal structural variation and terminal group transformation of samples with different treatments. As depicted in Figs. 2e and S13, the (002) peak shifting from 9.5° to a lower angle of 8.9° indicated the successful fabrication of $\text{Ti}_3\text{C}_2\text{T}_x$ due to the removal of the Al element and the introduction of terminal groups. After hydrothermal oxidation, the diffraction peak of $\sim 25.2^\circ$ emerged due to the existence of TiO_2 [39]. In addition, the XRD patterns of 3D-networked $\text{Ti}_3\text{C}_2\text{T}_x\text{-TiO}_2$ confirm that

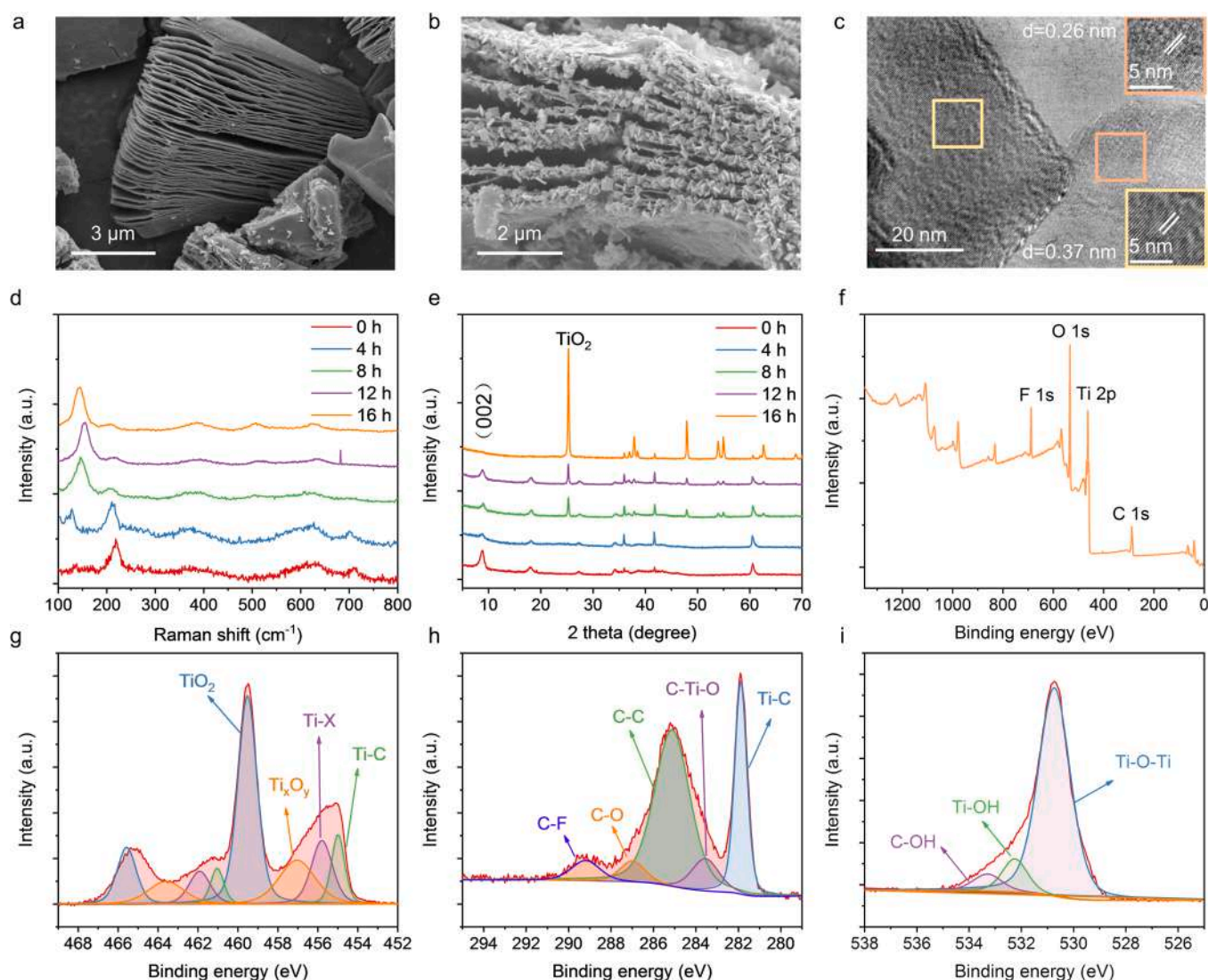


Fig. 2. Characterization of different functional materials. a, b, SEM images of $\text{Ti}_3\text{C}_2\text{T}_x$ (a) and 3D-networked $\text{Ti}_3\text{C}_2\text{T}_x\text{-TiO}_2$ heterostructure (magnification in 15,000 times) (b). c, HRTEM image of 3D-networked $\text{Ti}_3\text{C}_2\text{T}_x\text{-TiO}_2$. The inset yellow and orange image shows the indexed FFT image of $\text{Ti}_3\text{C}_2\text{T}_x$ and TiO_2 , respectively. d, Raman patterns of 3D-networked $\text{Ti}_3\text{C}_2\text{T}_x\text{-TiO}_2$ heterostructure for different oxidation times. e, XRD patterns of 3D-networked $\text{Ti}_3\text{C}_2\text{T}_x\text{-TiO}_2$ heterostructure for different oxidation times. f–i, XPS survey of fabricated 3D-networked $\text{Ti}_3\text{C}_2\text{T}_x\text{-TiO}_2$ heterostructure (f) and the core level spectrum of Ti 2p (g), C 1s (h), and O 1s (i).

the crystal phase of TiO_2 is anatase phase. Meanwhile, the diffraction intensity increased with the extension of oxidation time, indicating an increase in TiO_2 content, which was consistent with the SEM results. Similarly, the XPS results showed a significant change before (Fig. S14) and after oxidation (Fig. 2f–i), indicating the formation of $\text{Ti}_3\text{C}_2\text{T}_x\text{-TiO}_2$ heterostructure [31]. To clearly characterize the surface terminal of $\text{Ti}_3\text{C}_2\text{T}_x\text{-TiO}_2$ heterostructure for different oxidation times, the detailed XPS data were shown in Fig. S15, and the detailed description can be found in Supplementary Note 1. In addition, the contrast material of particulate TiO_2 coated onto $\text{Ti}_3\text{C}_2\text{T}_x$ to constitute the $\text{Ti}_3\text{C}_2\text{T}_x\text{-TiO}_2(\text{p})$ heterostructure was fabricated without the morphology directing reagent NaBF_4 to confirm this controllable *in-situ*-oxidization strategy. The detailed fabrication process and the characterization can be found in the experimental section and Figs. S16–S17.

As a photoelectric conversion device, the performance of photodetectors was influenced by both the optical and electrical properties of

functional materials. Based on this, we first characterized the optical and electrical properties of the fabricated $\text{Ti}_3\text{C}_2\text{T}_x\text{-TiO}_2$ heterostructure with the help of a semiconductor test platform and UV–vis spectrophotometer. As can be seen from Figs. 3a–b, both the optical and electrical properties of functional materials are closely related to the oxidation time. The formation of 3D-networked $\text{Ti}_3\text{C}_2\text{T}_x\text{-TiO}_2$ promotes optical absorption but suppresses carrier transport at the same time. Due to the trade-off between electrical and optical properties, when the oxidation time was 4 h, the decreased conductivity and limited enhanced optical absorption induced by the slightly damaged structure of $\text{Ti}_3\text{C}_2\text{T}_x$ and weak oxidation degree result in the whole photoelectric performance of the materials degraded. Further oxidation of $\text{Ti}_3\text{C}_2\text{T}_x$ leads to the formation of the 3D-networked $\text{Ti}_3\text{C}_2\text{T}_x\text{-TiO}_2$ heterostructure, whose increased excitation of photogenerated electron-hole pairs and improved electron collection efficiency can greatly improve the photoelectric performance, with the optimum performance reaching 0.71 nA

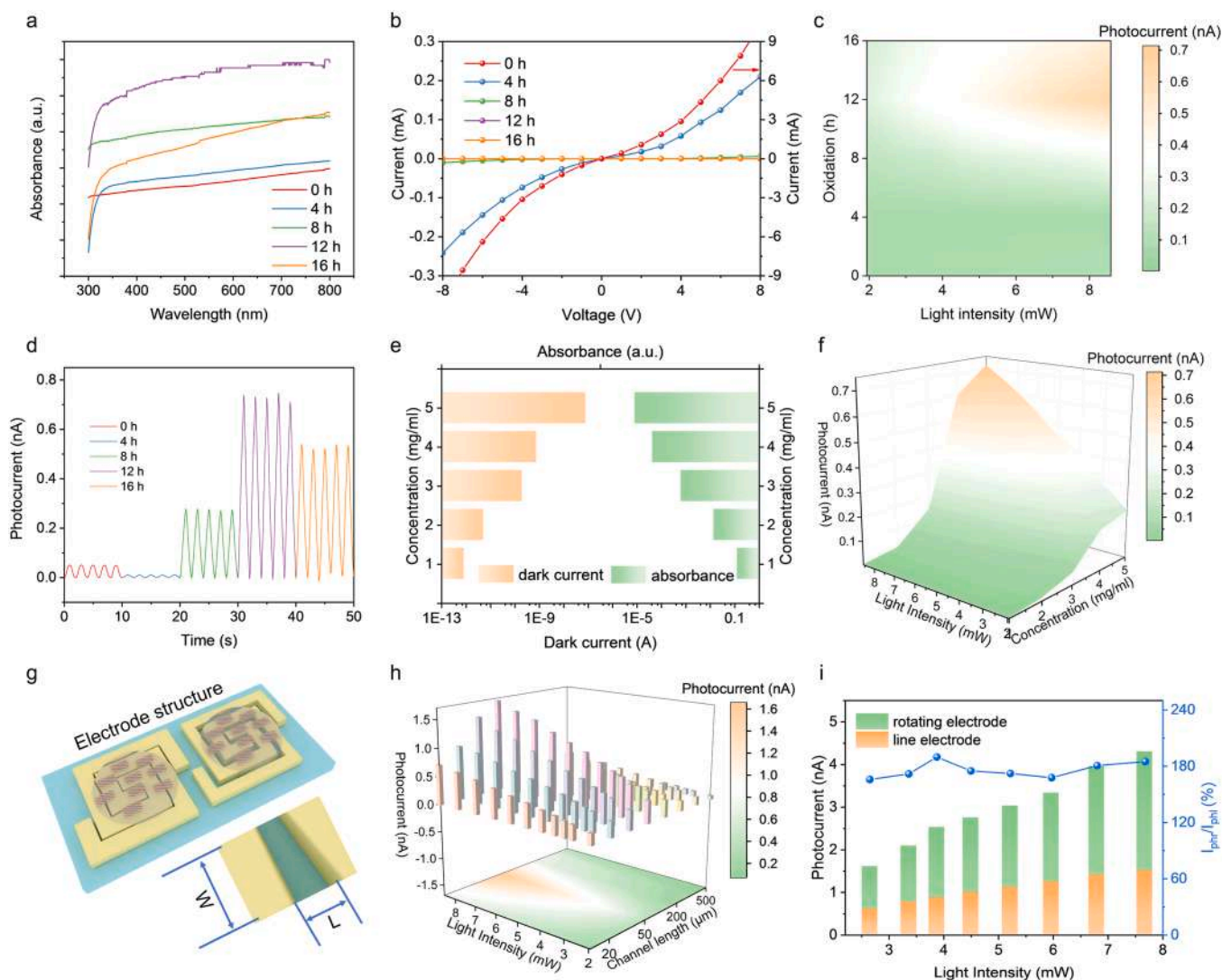


Fig. 3. Photoelectric performance of 3D-networked $\text{Ti}_3\text{C}_2\text{T}_x\text{-TiO}_2$ heterostructure. a, Optical absorption of 3D-networked $\text{Ti}_3\text{C}_2\text{T}_x\text{-TiO}_2$ heterostructure photodetectors for different oxidation times. b, Experimental I-V characteristics of 3D-networked $\text{Ti}_3\text{C}_2\text{T}_x\text{-TiO}_2$ heterostructure photodetectors for different oxidation times. c, Photoresponse behaviors of 3D-networked $\text{Ti}_3\text{C}_2\text{T}_x\text{-TiO}_2$ heterostructure photodetectors for different light intensity of 405 nm light illumination at 5 V bias. d, Time-dependent photocurrent of 3D-networked $\text{Ti}_3\text{C}_2\text{T}_x\text{-TiO}_2$ heterostructure photodetectors for different oxidation times under the 405 nm light illumination (8.58 mW) at 5 V bias. e, Dark current at 5 V bias and optical absorption at 405 nm of 3D-networked $\text{Ti}_3\text{C}_2\text{T}_x\text{-TiO}_2$ heterostructure with different concentrations. f, Photoresponse behaviors of the 3D-networked $\text{Ti}_3\text{C}_2\text{T}_x\text{-TiO}_2$ heterostructure photodetectors with different concentrations under different light intensity of 405 nm light illumination at 5 V bias. g, Schematic diagram of electrode configurations varying the channel length and the channel width. h, Photoresponse of the 3D-networked $\text{Ti}_3\text{C}_2\text{T}_x\text{-TiO}_2$ heterostructure photodetectors for 12 h oxidation time with different channel lengths under the different light intensity of 405 nm light illumination at 5 V bias. i, Photoresponse comparison of 3D-networked $\text{Ti}_3\text{C}_2\text{T}_x\text{-TiO}_2$ heterostructure photodetectors for 12 h oxidation time with different electrode configurations under the 405 nm light illumination (8.58 mW) at 5 V bias.

under 405 nm (8.58 mW) light illumination at 5 V bias when the oxidation time is 12 h. As the oxidation time was further increased to 16 h, the absorbance of $\text{Ti}_3\text{C}_2\text{T}_x$ decreased due to the lack of plasmonic absorption, while the conductivity also decreased, leading to a decrease in photocurrent as well, and the detailed tendency of photocurrent with the oxidation time was shown in Fig. 3c–d. The detailed dark current and photocurrent at 5 V bias under 405 nm light illumination (8.58 mW), the calculated responsivity and detectivity of the different photodetectors were included in Table S1. As a result, the output performance was enhanced by 13.3 times compared with the pristine $\text{Ti}_3\text{C}_2\text{T}_x$ photodetectors. Based on the results of photocurrent measurement, the photoresponsivity and detectivity can be evaluated to be 0.078 mA/W and 8.40×10^4 Jones, the detailed calculation process can be found in Supplementary Note 2.

Further analysis shows that the enhanced photoelectric performance of the designed 3D-networked $\text{Ti}_3\text{C}_2\text{T}_x\text{-TiO}_2$ heterostructure photodetectors is attributed to the following reasons: firstly, the increased excitation of photogenerated electron-hole pairs can be prompted in both $\text{Ti}_3\text{C}_2\text{T}_x$ and derivative TiO_2 . Secondly, it is reported that the fast carrier transfer process can occur in $\text{Ti}_3\text{C}_2\text{T}_x\text{-TiO}_2$ heterostructure [36]. The 2D TiO_2 nanosheets can bridge the separated $\text{Ti}_3\text{C}_2\text{T}_x$ nanosheets to form the 3D network, which provides more efficient conductive pathways to further facilitate the carrier separate and transport [36]. As for the contrast material of $\text{Ti}_3\text{C}_2\text{T}_x\text{-TiO}_2(\text{p})$, when the separated $\text{Ti}_3\text{C}_2\text{T}_x$ nanosheets are not connected by TiO_2 nanosheets, the increased electron-hole pairs cannot be effectively collected for the lack of sufficient conductive paths (Fig. S18), and therefore the photodetectors show the relatively low photoresponsivity of 0.012 mA/W, as shown in Fig. S19. On this basis, we utilized the time-resolved photoluminescence (TRPL) to provide insight into the species' excited state dynamics, as shown in Fig. S20. The decay traces were fitted using a two-exponential decay model [40], and the detailed model can be found in Supplementary Note 3 and the parameters were listed in Table S2. Compared with the $\text{Ti}_3\text{C}_2\text{T}_x\text{-TiO}_2(\text{p})$, the 3D-networked $\text{Ti}_3\text{C}_2\text{T}_x\text{-TiO}_2$ heterostructure shows a shorter average PL lifetime, which suggested an efficient carrier transport pathway between the $\text{Ti}_3\text{C}_2\text{T}_x$ and TiO_2 nanosheets. Similarly, when the 3D-networked $\text{Ti}_3\text{C}_2\text{T}_x\text{-TiO}_2$ heterostructure photodetector for 12 h oxidation time was placed in air for one month, the photocurrent would drop to 0.047 nA under the same condition (Fig. S21), which is attribute to the broken of 3D-networked structure as shown in Fig. S22. Lastly, the derivative TiO_2 nanosheets coated on the surface of MXenes can insulate water and oxygen, which may contribute to the good stability of photodetectors [38]. As shown in Fig. S23a, the performance showed almost no degradation after 300 cycles of repetitive irradiation of 0.5 Hz with a 405 nm laser. In addition, its photocurrent remains unchanged after 5000 s of light illumination (Fig. S23b), further confirming its long-term stability. Therefore, the designed 3D-networked $\text{Ti}_3\text{C}_2\text{T}_x\text{-TiO}_2$ photodetector exhibits better performance and can be applied in practical applications.

The detailed photoelectric performance of the optimum devices was further characterized as shown in Figs. S24a–b. From the time-dependent photoresponse of the 3D-networked $\text{Ti}_3\text{C}_2\text{T}_x\text{-TiO}_2$ heterostructure, the photocurrent increases linearly with the increase of light intensity. Furthermore, the response speed of photodetectors can be obtained from the enlarged time-dependent photoresponse in Fig. S24c. The rise/fall time of photodetectors, defined as the time required to increase/decrease from 10% to 90% of its peak photocurrent, was 0.694/0.812 s respectively, which is faster than that of the reported $\text{Ti}_3\text{C}_2\text{T}_x\text{-TiO}_2$ composites [30]. For the sharp peak of photocurrent, we measured the photoelectric performance under the same illumination with different on-off times (Fig. S25a). The photocurrent can be further increased to 1.37 nA when the on-off time is extended to 100 s. In addition, the wide bandgap of TiO_2 (3.2–3.3 eV) results in the optical absorption in the UV range. From the photoelectric performance under 365 nm light illumination (Fig. S25b), it can be found that the higher photocurrent can be obtained despite the relatively low light intensity,

indicating the possibility in the field of UV applications. Lastly, bending stability is an important criterion to evaluate its flexibility. The detailed bending angle and bending radius of the flexible device are quantified in the same way the same as those reported papers [41,42], as shown in Fig. S26a. It clearly shows that 70.6% of its initial photocurrent can be maintained even at a large bending angle as well as 79.7% of the initial properties after 1500 bending cycles, evidently presenting the excellent flexibility of flexible photodetectors (Figs. S26b–c).

Furthermore, the regulation of solution concentration and electrode structure was put forward to modulate the photoelectric performance. As can be seen from Fig. 3e and Fig. S27, both the optical absorption and the dark current increase with the solution concentration, illustrating the increased photogenerated electron-hole pairs and carrier transport capacity. As a result, the device with the solution concentration of 5 mg/mL exhibits the improved photocurrent of 0.71 nA under 405 nm (8.58 mW) light illumination at 5 V bias (Fig. 3f). On the other hand, the width and length of the channel also seriously affect the performance of the devices (Fig. 3g). From the I-V curve depicted in Fig. S28, it is clear that the current decreased with the increase of channel length, indicating the suppressed carrier transport. On the contrary, the optical absorption would increase because of the addition of functional materials. The test results show that the photocurrent tends to increase and then decrease as the channel length increases (Fig. 3h), and the device performs best when the channel length is 50 μm . Apart from the channel length, the effect of device channel width on performance has also been investigated. The electrode structure was regulated from line electrode to rotating electrode to widen the channel width while keeping constant channel length (Fig. S29), which induced more optical absorption because of the increased content of functional materials between electrodes. The output of the photodetectors based on the line electrode and rotating electrode is defined as I_{phl} and I_{phr} , respectively. As a result, the photoelectric performance can be enhanced to 180% of the original output after the electrode structure change, as shown by the blue dotted line in Fig. 3i. In this way, excellent performance can be obtained via adjusting the concentration of functional materials and adopting specific electrode configurations, which promotes its application in the field of optical imaging.

To demonstrate the application of optical imaging, a flexible photodetectors array consisting of 11×11 pixels was fabricated onto a paper substrate of 10×10 cm to verify the visual imaging capability. As shown in Fig. 4a, in virtue of the white spotlight and a patterned mask, light is shone onto the photodetectors array in the shape of the mask, such as letters or graphs. In this case, the photoelectric output of all irradiated photodetectors will change from low level to high level, while the photoelectric output of unirradiated photodetectors will remain unchanged. According to the photoelectric output of all photodetectors, the shape of the mask can be accurately restored by the photodetectors array. Fig. 4b–d illustrate the whole fabricating process of photodetectors array, including magnetron sputtering, direct ultraviolet laser cutting, and drop coating, and the resulting photodetectors array is shown in Fig. 4e, which reveals the possibility of large-area and high-resolution imaging on rigid or flexible substrates.

On this basis, different letters and graph patterned masks were fabricated to produce the patterned light to verify the functionality of letter imaging and complex graphic imaging as shown in Fig. 4g. After the analysis of the photoelectric output gotten by a low-noise current preamplifier, the “p” letter pattern can be successfully restored, as shown in Fig. 4h, and the time-dependent photoresponse of photodetectors (X axis=3) can be found in Fig. 4f. Moreover, a more complex circular pattern imaging can also be achieved by the photodetectors array as demonstrated in Fig. 4i. (The detailed photoelectric output of each photodetector can be found in Fig. S30.) Combined with the advanced equipment and processes, the photodetectors array with higher resolution can be easily fabricated as shown in Fig. S31. Undoubtedly, the proposed method allows the fabrication of a larger area and higher resolution photodetectors array to distinguish and restore

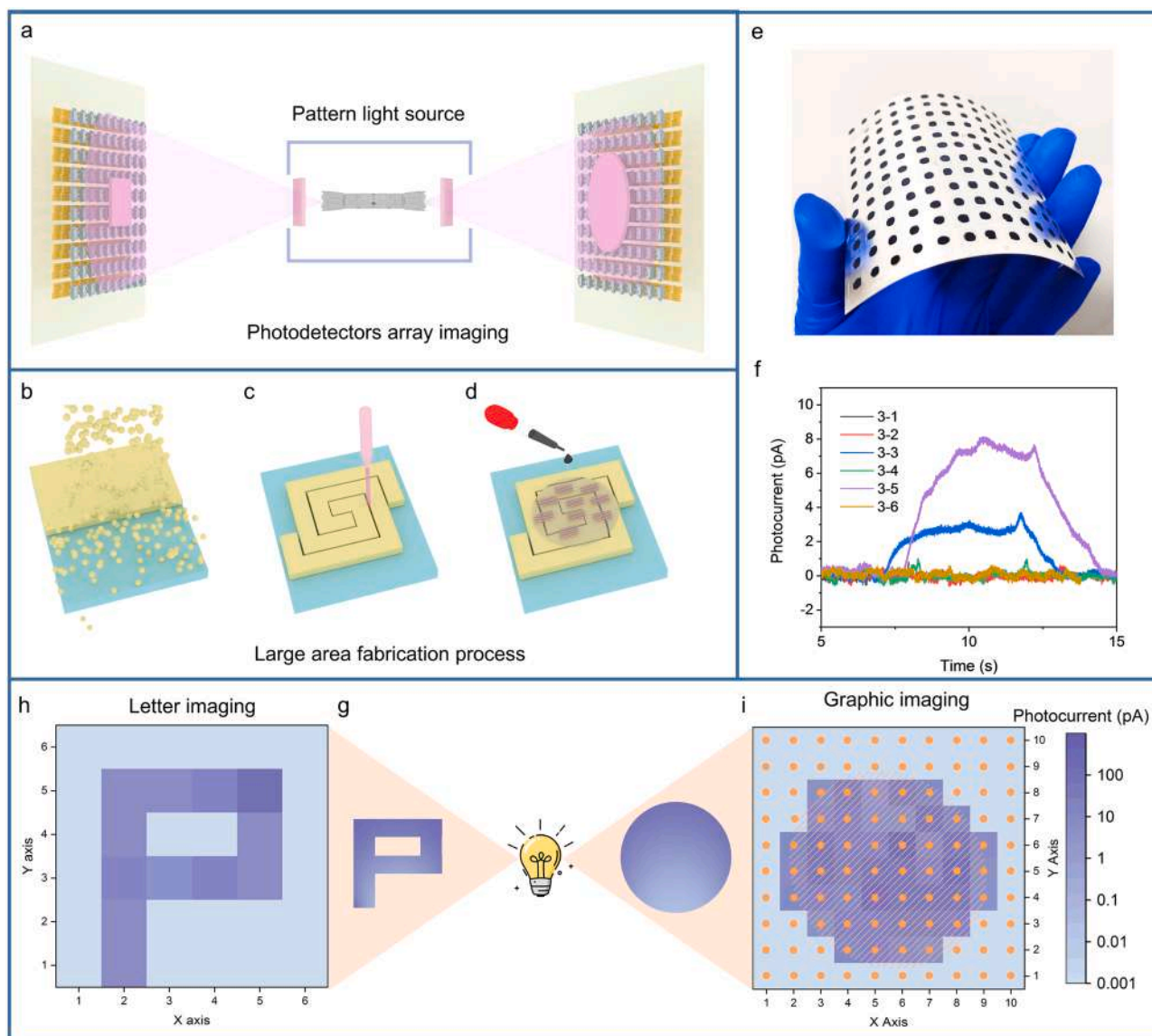


Fig. 4. Optical imaging application of photodetectors based on 3D-networked $\text{Ti}_3\text{C}_2\text{T}_x\text{-TiO}_2$ heterostructure. a, Schematic illustration of the 3D-networked $\text{Ti}_3\text{C}_2\text{T}_x\text{-TiO}_2$ heterostructure photodetectors for optical imaging, including light source, patterned mask, and photodetectors array. b–d, Schematic illustration of the 3D-networked $\text{Ti}_3\text{C}_2\text{T}_x\text{-TiO}_2$ heterostructure photodetectors array with the help of radio frequency magnetron sputtering technology (b), direct ultraviolet laser cutting (c), and drop-casting technology (d). e, Digital photo of the photodetectors array on flexible paper substrate. f, Time-dependent photoresponse of photodetector array under the white spotlight with “p” mask (X axis = 3). g–i, Applications of the photodetectors array based on 3D-networked $\text{Ti}_3\text{C}_2\text{T}_x\text{-TiO}_2$ heterostructure in optical imaging of letter “p” and circular graph.

images, which provides a viable method for achieving optical imaging.

3. Conclusions

In summary, we have designed a 3D-networked $\text{Ti}_3\text{C}_2\text{T}_x\text{-TiO}_2$ photodetector *via* a simple controllable *in-situ*-oxidization strategy and demonstrated its prospects in large-area optical imaging. Taking advantage of the intrinsic instability of $\text{Ti}_3\text{C}_2\text{T}_x$ and morphology directing reagent, the 3D-networked $\text{Ti}_3\text{C}_2\text{T}_x\text{-TiO}_2$ heterostructure was successfully constructed to achieve superior photoelectric performance. Due to its enhanced optical absorption and higher electrical collection efficiency, the designed photodetector exhibits 13.3 times performance improvement. Based on this, optical imaging of letters and circular patterns was successfully demonstrated by photodetectors array (11×11 pixels) fabricated on a flexible paper substrate of $10 \times 10 \text{ cm}^2$. The proposed controllable *in-situ*-oxidization strategy of 3D-networked heterostructure construction provides a feasible approach to achieve

high-performance MXene-based photodetectors, thus creating a new opportunity for optical imaging in the future.

4. Experimental section

4.1. The fabrication of $\text{Ti}_3\text{C}_2\text{T}_x$ nanosheets

The basic functional materials $\text{Ti}_3\text{C}_2\text{T}_x$ nanosheets were synthesized by the chemical etching of Ti_3AlC_2 (2.5 g) *via* the etchant HF (25 mL 40 wt%) with magnetic stirring at 40°C for 24 h. After that, the suspension was washed by centrifuge at 4000 rpm several times until the pH of the supernate at around 6. The sediment of the production was collected and vacuum dried at 40°C for further hydrothermal oxidation.

4.2. The preparation of 3D-networked $\text{Ti}_3\text{C}_2\text{T}_x\text{-TiO}_2$ heterostructure

The $\text{Ti}_3\text{C}_2\text{T}_x\text{-TiO}_2$ heterostructure was fabricated *via* a simple

hydrothermal method with the help of morphology directing reagent. In detail, 0.1 g etching product was added into 15 mL of 1 M HCl solution that contains the morphology directing reagent NaBF₄ (0.165 g). After that, the suspension was stirred for 30 min *via* the magnetic stirrer and ultrasonic for another 10 min. Then, transferring the solution into a Teflon-lined stainless steel autoclave to take the hydrothermal oxidation process at 160 °C for 4–16 h.

The contrast materials of Ti₃C₂T_x-TiO₂(p) heterostructure was fabricated using the same hydrothermal method for the lack of NaBF₄. And the solution used in this process was changed into 15 mL deionized water.

4.3. The preparation of photodetectors

First of all, the Ag electrode was obtained *via* the radio frequency magnetron sputtering technology. And the designed electrode structure and channel length were incised by UV cold laser processing technology. The 10 μL fabricated functional materials with different concentrations were dropped onto the electrode and dried at ambient temperature for further measurement.

4.4. Characterizations

The morphology and element distribution were characterized using a field emission scanning electron microscope (JSM-7800F) and transmission electron microscopy (JEM-2100F). The crystal structure of the functional materials was characterized by X-ray diffraction using Cu Kα radiation. XPS (ESCALAB XI +) and Raman spectroscopy (HORIBA Jobin-Yvon XploRA ONE, 532 nm laser) were adopted to analyze and monitor the surface terminations of functional materials. The orbital energies were characterized by the UPS (ESCALAB XI +). The optical absorption properties were characterized *via* the UV–vis absorption spectrum (Techcomp UV2310II). The electrical properties were characterized by the Keithley 4200 semiconductor testing system and Stanford SR570 preamplifier. The time-resolved photoluminescence (TRPL) spectra were characterized by a 405 nm pulse laser as an excitation source with FLS980. The light intensity of the laser was controlled *via* the function signal generator.

CRedit authorship contribution statement

Da Xiong: Conceptualization, Methodology, Formal analysis, Investigation, Visualization, Writing – original draft, Supervision. **Weili Deng:** Conceptualization, Visualization, Writing – review & editing, Funding acquisition. **Guo Tian:** Investigation, Visualization. **Binbin Zhang:** Methodology, Investigation. **Shen Zhong:** Investigation, **Yanting Xie:** Investigation, Formal analysis. **Tao Yang:** Investigation. **Haibo Zhao:** Investigation. **Weiqing Yang:** Writing – review & editing, Funding acquisition, Supervision.

Declaration of Competing Interest

The authors declare that they have no known competing financial interests or personal relationships that could have appeared to influence the work reported in this paper.

Acknowledgements

This work was supported by the National Natural Science Foundation of China (No. 61801403), the Sichuan Province Foundation of Distinguished Young Team (No. 20CXTD0106), and the Basic Research Cultivation Project (No. 2682021ZTPY004). We are thankful for the help from the Analysis and Testing Center of Southwest Jiaotong University.

Appendix A. Supporting information

Supplementary data associated with this article can be found in the online version at [doi:10.1016/j.nanoen.2021.106889](https://doi.org/10.1016/j.nanoen.2021.106889).

References

- [1] M. Rein, V.D. Favrod, C. Hou, T. Khudiyev, A. Stolyarov, J. Cox, C.C. Chung, C. Chhav, M. Ellis, J. Joannopoulos, Y. Fink, Diode fibres for fabric-based optical communications, *Nature* 560 (2018) 214–218, <https://doi.org/10.1038/s41586-018-0390-x>.
- [2] D. Xiong, W. Deng, G. Tian, Y. Gao, X. Chu, C. Yan, L. Jin, Y. Su, W. Yan, W. Yang, A piezo-phototronic enhanced serrate-structured ZnO-based heterojunction photodetector for optical communication, *Nanoscale* 11 (2019) 3021–3027, <https://doi.org/10.1039/c8nr09418g>.
- [3] W. Wu, X. Wang, X. Han, Z. Yang, G. Gao, Y. Zhang, J. Hu, Y. Tan, A. Pan, C. Pan, Flexible photodetector arrays based on patterned CH₃NH₃PbI_{3-x}Cl_x perovskite film for real-time photosensing and imaging, *Adv. Mater.* 31 (2018), 1805913, <https://doi.org/10.1002/adma.201805913>.
- [4] W. Deng, H. Huang, H. Jin, W. Li, X. Chu, D. Xiong, W. Yan, F. Chun, M. Xie, C. Luo, L. Jin, C. Liu, H. Zhang, W. Deng, W. Yang, All-sprayed-processable, large-area, and flexible perovskite/MXene-based photodetector arrays for photocommunication, *Adv. Opt. Mater.* 7 (2019), 1801521, <https://doi.org/10.1002/adom.201801521>.
- [5] W. Zhou, Y. Shang, F.P. García de Arquer, K. Xu, R. Wang, S. Luo, X. Xiao, X. Zhou, R. Huang, E.H. Sargent, Z. Ning, Solution-processed upconversion photodetectors based on quantum dots, *Nat. Electron.* 3 (2020) 251–258, <https://doi.org/10.1038/s41928-020-0388-x>.
- [6] W. Wei, Y. Zhang, Q. Xu, H. Wei, Y. Fang, Q. Wang, Y. Deng, T. Li, A. Gruverman, L. Cao, J. Huang, Monolithic integration of hybrid perovskite single crystals with heterogeneous substrate for highly sensitive X-ray imaging, *Nat. Photon.* 11 (2017) 315–321, <https://doi.org/10.1038/nphoton.2017.43>.
- [7] E.O. Polat, G. Mercier, I. Nikitskiy, E. Puma, T. Galan, S. Gupta, M. Montagu, J. J. Piqueras, M. Bouwens, T. Durduran, G. Konstantatos, S. Goossens, F. Koppens, Flexible graphene photodetectors for wearable fitness monitoring, *Sci. Adv.* 5 (2019), eaaw7846, <https://doi.org/10.1126/sciadv.aaw7846>.
- [8] J. Kim, M. Kim, M.S. Lee, K. Kim, S. Ji, Y.T. Kim, J. Park, K. Na, K.H. Bae, H. Kyun Kim, F. Bien, C. Young Lee, J.U. Park, Wearable smart sensor systems integrated on soft contact lenses for wireless ocular diagnostics, *Nat. Commun.* 8 (2017) 14997, <https://doi.org/10.1038/ncomms14997>.
- [9] K.F. Mak, J. Shan, Photonics and optoelectronics of 2D semiconductor transition metal dichalcogenides, *Nat. Photon.* 10 (2016) 216–226, <https://doi.org/10.1038/nphoton.2015.282>.
- [10] J.D. Yao, Z.Q. Zheng, G.W. Yang, Production of large-area 2D materials for high-performance photodetectors by pulsed-laser deposition, *Prog. Mater. Sci.* 106 (2019), 100573, <https://doi.org/10.1016/j.pmatsci.2019.100573>.
- [11] M. Naguib, M. Kurtoglu, V. Presser, J. Lu, J. Niu, M. Heon, L. Hultman, Y. Gogotsi, M.W. Barsoum, Two-dimensional nanocrystals produced by exfoliation of Ti₃AlC₂, *Adv. Mater.* 23 (2011) 4248–4253, <https://doi.org/10.1002/adma.201102306>.
- [12] K. Hantanasirisakul, Y. Gogotsi, Electronic and optical properties of 2D transition metal carbides and nitrides (MXenes), *Adv. Mater.* 30 (2018), 1804779, <https://doi.org/10.1002/adma.201804779>.
- [13] A. VahidMohammadi, J. Rosen, Y. Gogotsi, The world of two-dimensional carbides and nitrides (MXenes), *Science* 372 (2021) eaabf1581, <https://doi.org/10.1126/science.aabf1581>.
- [14] C. Ma, M.-G. Ma, C. Si, X.-X. Ji, P. Wan, Flexible MXene-based composites for wearable devices, *Adv. Funct. Mater.* 31 (2021), 2009524, <https://doi.org/10.1002/adfm.202009524>.
- [15] T. Schultz, N.C. Frey, K. Hantanasirisakul, S. Park, S.J. May, V.B. Shenoy, Y. Gogotsi, N. Koch, Surface termination dependent work function and electronic properties of Ti₃C₂T_x MXene, *Chem. Mater.* 31 (2019) 6590–6597, <https://doi.org/10.1021/acs.chemmater.9b00414>.
- [16] A. Agresti, A. Pazniak, S. Pescetelli, A. Di Vito, D. Rossi, A. Pecchia, M. Auf der Maur, A. Liedl, R. Larciprete, D.V. Kuznetsov, D. Saranin, A. Di Carlo, Titanium-carbide MXenes for work function and interface engineering in perovskite solar cells, *Nat. Mater.* 18 (2019) 1228–1234, <https://doi.org/10.1038/s41563-019-0478-1>.
- [17] E. Quain, T.S. Mathis, N. Kurra, K. Maleski, K.L. Van Aken, M. Alhabeib, H. N. Alshareef, Y. Gogotsi, Direct writing of additive-free MXene-in-water ink for electronics and energy storage, *Adv. Mater. Technol.* 4 (2019), 1800256, <https://doi.org/10.1002/admt.201800256>.
- [18] J. Zhang, N. Kong, S. Uzun, A. Levitt, S. Seyedin, P.A. Lynch, S. Qin, M. Han, W. Yang, J. Liu, X. Wang, Y. Gogotsi, J.M. Raza, Scalable manufacturing of free-standing, strong Ti₃C₂T_x MXene films with outstanding conductivity, *Adv. Mater.* 32 (2020), 2001093, <https://doi.org/10.1002/adma.202001093>.
- [19] C.E. Shuck, Y. Gogotsi, Taking MXenes from the lab to commercial products, *Chem. Eng. J.* 401 (2020), 125786, <https://doi.org/10.1016/j.cej.2020.125786>.
- [20] K. Montazeri, M. Currie, L. Verger, P. Dianat, M.W. Barsoum, B. Nabet, Beyond gold: spin-coated Ti₃C₂-based MXene photodetectors, *Adv. Mater.* 31 (2019), 1903271, <https://doi.org/10.1002/adma.201903271>.
- [21] W. Song, J. Chen, Z. Li, X. Fang, Self-powered MXene/GaN van der Waals heterojunction ultraviolet photodiodes with superhigh efficiency and stable current outputs, *Adv. Mater.* 33 (2021), 2101059, <https://doi.org/10.1002/adma.202101059>.

- [22] Z. Kang, Y. Ma, X. Tan, M. Zhu, Z. Zheng, N. Liu, L. Li, Z. Zou, X. Jiang, T. Zhai, Y. Gao, MXene-silicon van der Waals heterostructures for high-speed self-driven photodetectors, *Adv. Electron. Mater.* 3 (2017), 1700165, <https://doi.org/10.1002/aelm.201700165>.
- [23] H.C. Fu, V. Ramalingam, H. Kim, C.H. Lin, X. Fang, H.N. Alshareef, J.H. He, MXene-contacted silicon solar cells with 11.5% efficiency, *Adv. Energy Mater.* 9 (2019), 1900180, <https://doi.org/10.1002/aenm.201900180>.
- [24] H. Xu, A. Ren, J. Wu, Z. Wang, Recent advances in 2D MXenes for photodetection, *Adv. Funct. Mater.* 30 (2020), 2000907, <https://doi.org/10.1002/adfm.202000907>.
- [25] J. Chen, Z. Li, F. Ni, W. Ouyang, X. Fang, Bio-inspired transparent MXene electrodes for flexible UV photodetectors, *Mater. Horiz.* 7 (2020) 1828–1833, <https://doi.org/10.1039/d0mh00394h>.
- [26] Y. Xie, P.R.C. Kent, Hybrid density functional study of structural and electronic properties of functionalized $Ti_{n+1}X_n(X=C, N)$ monolayers, *Phys. Rev. B* 87 (2013), 235441, <https://doi.org/10.1103/PhysRevB.87.235441>.
- [27] M. Khazaei, A. Ranjbar, M. Arai, T. Sasaki, S. Yunoki, Electronic properties and applications of MXenes: a theoretical review, *J. Mater. Chem. C* 5 (2017) 2488–2503, <https://doi.org/10.1039/c7tc00140a>.
- [28] A.D. Dillon, M.J. Ghidui, A.L. Krick, J. Griggs, S.J. May, Y. Gogotsi, M.W. Barsoum, A.T. Fafarman, Highly conductive optical quality solution-processed films of 2D titanium carbide, *Adv. Funct. Mater.* 26 (2016) 4162–4168, <https://doi.org/10.1002/adfm.201600357>.
- [29] A. Pan, X. Ma, S. Huang, Y. Wu, M. Jia, Y. Shi, Y. Liu, P. Wangyang, L. He, Y. Liu, CsPbBr₃ perovskite nanocrystal grown on MXene nanosheets for enhanced photoelectric detection and photocatalytic CO₂ reduction, *J. Phys. Chem. Lett.* 10 (2019) 6590–6597, <https://doi.org/10.1021/acs.jpcclett.9b02605>.
- [30] S. Chertopalov, V.N. Mochalin, Environment-sensitive photoresponse of spontaneously partially oxidized Ti₃C₂ MXene thin films, *ACS Nano* 12 (2018) 6109–6116, <https://doi.org/10.1021/acsnano.8b02379>.
- [31] C. Peng, X. Yang, Y. Li, H. Yu, H. Wang, F. Peng, Hybrids of two-dimensional Ti₃C₂ and TiO₂ exposing {001} facets toward enhanced photocatalytic activity, *ACS Appl. Mater. Interfaces* 8 (2016) 6051–6060, <https://doi.org/10.1021/acsmi.5b11973>.
- [32] H.S. Jung, G.S. Han, N.-G. Park, M.J. Ko, Flexible perovskite solar cells, *Joule* 3 (2019) 1850–1880, <https://doi.org/10.1016/j.joule.2019.07.023>.
- [33] C. Liu, C. Xiao, C. Xie, W. Li, Flexible organic solar cells: materials, large-area fabrication techniques and potential applications, *Nano Energy* 89 (2021), 106399, <https://doi.org/10.1016/j.nanoen.2021.106399>.
- [34] Y. Zhang, L. Zhang, K. Cui, S. Ge, X. Cheng, M. Yan, J. Yu, H. Liu, Flexible electronics based on micro/nanostructured paper, *Adv. Mater.* 30 (2018), 1801588, <https://doi.org/10.1002/adma.201801588>.
- [35] M. Naguib, O. Mashtalir, M.R. Lukatskaya, B. Dyatkin, C. Zhang, V. Presser, Y. Gogotsi, M.W. Barsoum, One-step synthesis of nanocrystalline transition metal oxides on thin sheets of disordered graphitic carbon by oxidation of MXenes, *Chem. Commun.* 50 (2014) 7420–7423, <https://doi.org/10.1039/c4cc01646g>.
- [36] S. Debou, T. Zhang, X. Liu, F. Song, Y. Qian, J. Han, K. Maleski, Z.B. Zander, W. R. Creasy, D.L. Kuhn, Y. Gogotsi, B.G. DeLacy, Y. Rao, Charge dynamics in TiO₂/MXene composites, *J. Phys. Chem. C* 125 (2021) 10473–10482, <https://doi.org/10.1021/acs.jpcc.1c01543>.
- [37] S. Tu, Q. Jiang, X. Zhang, H.N. Alshareef, Large dielectric constant enhancement in MXene percolative polymer composites, *ACS Nano* 12 (2018) 3369–3377, <https://doi.org/10.1021/acsnano.7b08895>.
- [38] C.J. Zhang, S. Pinilla, N. McEvoy, C.P. Cullen, B. Anasori, E. Long, S.-H. Park, A. Seral-Ascaso, A. Shmeliov, D. Krishnan, C. Morant, X. Liu, G.S. Duesberg, Y. Gogotsi, V. Nicolosi, Oxidation stability of colloidal two-dimensional titanium carbides (MXenes), *Chem. Mater.* 29 (2017) 4848–4856, <https://doi.org/10.1021/acs.chemmater.7b00745>.
- [39] W. Yuan, L. Cheng, Y. An, S. Lv, H. Wu, X. Fan, Y. Zhang, X. Guo, J. Tang, Laminated hybrid junction of sulfur-doped TiO₂ and a carbon substrate derived from Ti₃C₂ MXenes: toward highly visible light-driven photocatalytic hydrogen evolution, *Adv. Sci.* 5 (2018), 1700870, <https://doi.org/10.1002/adv.201700870>.
- [40] X. Tang, Z. Zu, Z. Zang, Z. Hu, W. Hu, Z. Yao, W. Chen, S. Li, S. Han, M. Zhou, CsPbBr₃/reduced graphene oxide nanocomposites and their enhanced photoelectric detection application, *Sens. Actuators B* 245 (2017) 435–440, <https://doi.org/10.1016/j.snb.2017.01.168>.
- [41] K. Fukuda, K. Yu, T. Someya, The future of flexible organic solar cells, *Adv. Energy Mater.* 10 (2020), 2000765, <https://doi.org/10.1002/aenm.202000765>.
- [42] S. Cai, X. Xu, W. Yang, J. Chen, X. Fang, Materials and designs for wearable photodetectors, *Adv. Mater.* 31 (2019), 1808138, <https://doi.org/10.1002/adma.201808138>.